

RESEARCH

Open Access



Dynamic changes in 3D chromatin structure during male gametogenesis in *Arabidopsis thaliana*

Zhihan Song^{1†}, Qimin Xia^{2†}, Minqi Yang^{1†}, Tingting Yang^{1†}, Yali Liu³, Dingyue Wang¹, Jiayue Shu¹, Zhiyuan Liu^{2,4}, Yi Chi², Heming Xu², Dong Xing^{2,4*} and Yue Zhou^{1*} 

[†]Zhihan Song, Qimin Xia, Minqi Yang and Tingting Yang contributed equally to this work.

*Correspondence: dxing@pku.edu.cn; yue_zhou@pku.edu.cn

¹ State Key Laboratory of Gene Function and Modulation Research, School of Advanced Agricultural Sciences, Peking-Tsinghua Center for Life Sciences, Peking University, Beijing 100871, China

² Biomedical Pioneering Innovation Center (BIOPIC), School of Life Sciences, Peking University, Beijing 100871, China

³ Institute of Cell Biology and MOE Key Laboratory of Cell Activities and Stress Adaptations, School of Life Sciences, Lanzhou University, Lanzhou 730000, China

⁴ Beijing Advanced Innovation Center for Genomics (ICG), Peking University, Beijing 100871, China

Abstract

Background: Chromatin higher-order structure plays an important role in genome stability maintenance and gene transcriptional regulation; however, the dynamics of the three-dimensional (3D) chromatin in male gametophytes during the two rounds of mitosis remains elusive.

Results: Here, we use the optimized single-nucleus and low-input Hi-C methods to investigate changes in 3D chromatin structure in four types of male gametophyte nucleus at different stages. The reconstructed genome structures show that microspore nuclei develop towards two different directions. Although the 3D chromatin organization in generative nuclei is similar to that in microspore nuclei, vegetative nuclei lose chromosome territories, display dispersed centromeres, and switched A/B compartments, which are associated with vegetative specific gene expression. Additionally, we find that there is an active transcriptional center in sperm nuclei, emphasizing the transcription in *Arabidopsis* sperm is not completely inhibited despite the chromosomes being condensed.

Conclusions: Our data suggest that the special 3D structures of vegetative and sperm nuclei contribute to cell type-specific expression patterns.

Background

The 3D chromatin structure can be partitioned into chromosome territory, A/B compartments, topologically associating domains (TADs), and chromatin loops according to different spatial scales [1–3]. The ordered spatial distribution of chromatin is vital for the proper regulation of gene expression, since the 3D physical contacts can overcome the limitation of the linear arrangement of genes and regulatory elements on DNA at the one-dimensional level [4–6]. Several technologies and methods based on chromosome conformation capture (3C) have been used to study the 3D chromatin structure in mammals, *Drosophila*, and plants [4, 5, 7–12]. In recent years, the single-cell Hi-C



© The Author(s) 2025. **Open Access** This article is licensed under a Creative Commons Attribution-NonCommercial-NoDerivatives 4.0 International License, which permits any non-commercial use, sharing, distribution and reproduction in any medium or format, as long as you give appropriate credit to the original author(s) and the source, provide a link to the Creative Commons licence, and indicate if you modified the licensed material. You do not have permission under this licence to share adapted material derived from this article or parts of it. The images or other third party material in this article are included in the article's Creative Commons licence, unless indicated otherwise in a credit line to the material. If material is not included in the article's Creative Commons licence and your intended use is not permitted by statutory regulation or exceeds the permitted use, you will need to obtain permission directly from the copyright holder. To view a copy of this licence, visit <http://creativecommons.org/licenses/by-nc-nd/4.0/>.

(sc-Hi-C) and single-nucleus Hi-C (sn-Hi-C) techniques have been developed to study heterogeneity of 3D chromatin structure at single cell level, or 3D dynamics in rare sample, such as the zygote, in both animals and plants [5, 13–15]. Furthermore, the 3D genome structure can be reconstructed using a particle-on-a-string model to represent chromatin, which enables the performance of multi-omics analysis to more intuitively investigate the spatial relationship among transcription, epigenetic modifications, and 3D genome structure [5, 15]. Owing to these Hi-C-based methods, the molecular mechanisms underlying 3D chromatin regulation have gradually been revealed in many species. Chromosome territory constitutes a major feature of nuclear architecture in both animals and plants. Condensin II is reported to be involved in the chromosome territory configuration [16]. In addition, the chromosome could be partitioned into A and B compartments according to principal component (PC1) value [7]. A/B compartments have a close relationship with histone modifications and gene transcriptional activity [7, 14]. In mammals, H1 knock-down results in H3K27me3 reduction and H3K36me2 increase, which further leads to A/B compartments switching [17, 18]. However, there are very fewer compartments switched in *Arabidopsis h1s* mutants [19], which suggests that the mechanism underlying A/B compartment regulation is not conserved in plants and animals. In plants, chromatin remodeling complexes participate in the regulation of A/B compartments through the maintenance of H3K27me3 level [12]. Furthermore, the switching of A/B compartments in specific development stages facilitates the regulation of gene expression [20]. Moreover, CCCTC-binding factor (CTCF) functions as the organizer protein by binding to TAD boundaries in mammals [21]. In contrast to mammals, TAD boundaries in *Drosophila* prefer to be enriched with active histone modifications and insulator proteins instead of dCTCF [22]. Similar to the TADs in *Drosophila*, many studies have identified these domain structures in plants, which are also correlated with different histone modifications and therefore considered as the compartment domains (CDs) [11, 14, 22, 23]. In addition, the special nuclear structure, termed *KNOT*, has been identified in *Arabidopsis*, which is similar to the PIWI-interacting RNA cluster found in *Drosophila* [24].

Spermatogenesis or male gametogenesis is a crucial process for both animals and plants. In mammalian spermatogenesis, the round spermatid (1N) undergoes a series of morphological changes and developmental events to form the mature sperm (1N) [25–27]; however, flowering plants experience two special rounds of mitosis in male gametogenesis. The microspore (1N) experiences its first asymmetric division after meiosis to generate the generative (1N) and vegetative (1N) cells. Subsequently, the generative cell further divides to yield two sperm cells (1N). Vegetative cells mainly function to form the pollen tube which is responsible for the delivery of two mature sperm cells to fertilize with the egg cell and the central cell [28]. The two rounds of mitosis of haploid cells are the specific observation only existing in plants, which contributes to the study of the 3D genome structure changes in mitosis.

The development of the male germ cell is affected by multiple factors such as DNA methylation and histone modifications [29–34]. In plants, DNA methylation undergoes complex reprogramming during the development of male gametophytes, in which multiple mechanisms may be involved. For example, the transport of small interfering RNAs (siRNAs) from tapetal nurse cells to meiocytes can regulate germline gene expression

via the RNA-directed DNA methylation (RdDM) pathway [29, 31]. At the histone level, on the one hand, the loss of H3K27me3 facilitates the transcription of genes which are essential for spermatogenesis [30, 35, 36]; on the other hand, the chromatin bivalency with the acquisition of H3K27me3 and H3K4me3 in sperm nuclei has a close relationship with the distinct gene expression level. Meanwhile, the reduction of somatic H3K27me3 at developmental genes in sperm nuclei and marked H3K4me3 at genes required for pollination in vegetative nuclei facilitate each function during male gametogenesis [29, 30]. Moreover, histone variant H2B.8 has been reported to participate in the process of sperm nuclei compaction through phase separation [37].

The dynamic changes in 3D chromatin structure are also involved in male germ cell development. In mice and rhesus monkeys, the TADs re-configured and A/B compartments refined during meiosis [27, 38, 39]. Relevant study in rice roughly revealed the 3D genome structure of sperm nuclei [5]; however, the dynamics of 3D chromatin structure during the two rounds of mitosis in plant male gametogenesis remain elusive. Here, we combined the sn-Hi-C and low-input Hi-C methods to investigate the dynamic changes in 3D chromatin structure in microspore, generative, vegetative, and sperm nuclei. We described in detail how the 3D chromatin structure changed during gametogenesis from different dimensions, and demonstrated the correlation between distinct 3D chromatin structures and cell type-specific genes transcription.

Results

Chromatin structure reconfigures towards two directions during the two rounds of mitosis during male gametogenesis

To explore the 3D chromatin structure in four types of cells during male gametogenesis (Fig. 1a), we purified and isolated the nuclei from microspore (Additional File 1: Fig. S1), generative (Additional File 1: Fig. S2), vegetative, and sperm (Additional File 1: Fig. S3) cells using different methods. In brief, microspores were isolated by Fluorescence-Activated Cell Sorting (FACS) [40] and then further selected one by one under the microscope after moderate grinding (Additional File 1: Fig. S1). Bicellular pollen grains from *pHTR10::HTR10-RFP* maker line were also primarily isolated by cell size and autofluorescence using FACS (Additional File 1: Fig. S2a-e) [29], and then the generative nuclei were further sorted according to RFP signal with a second round of FACS (Additional File 1: Fig. S2f). The nuclei of vegetative and sperm cells were separated based on specific fluorescence using the *pMGH3::MGH3-eGFP/pACT11::H2B-mRFP* transgenic plants (Additional File 1: Fig. S3) [40]. We encapsulated single nucleus in gel matrix for subsequent enzyme digestion and ligation (Fig. 1b) [15, 41], and successfully sequenced 181 individual cells with a median of 41,684 chromatin contacts per cell (Additional file 2: Table S1). Among the 324 cells, 15 were microspores, 68 were generative nuclei, 118 were sperm nuclei, and 123 were vegetative nuclei. In addition, we performed modified low-input Hi-C (Fig. 1b) and obtained approximately 226 million, and 218 million contacts of three biological replicates in bulk vegetative and sperm nuclei, respectively (Additional File 1: Fig. S4). To make the bulk sample data comparable, we extracted 220 million contacts randomly from seedling Hi-C, which were used as the somatic control [11]. The contact counts are comparable with ones obtained from whole experiments in previous studies [42, 43]. Clustering of single nuclei based on Hi-C contact maps yielded 3 clusters

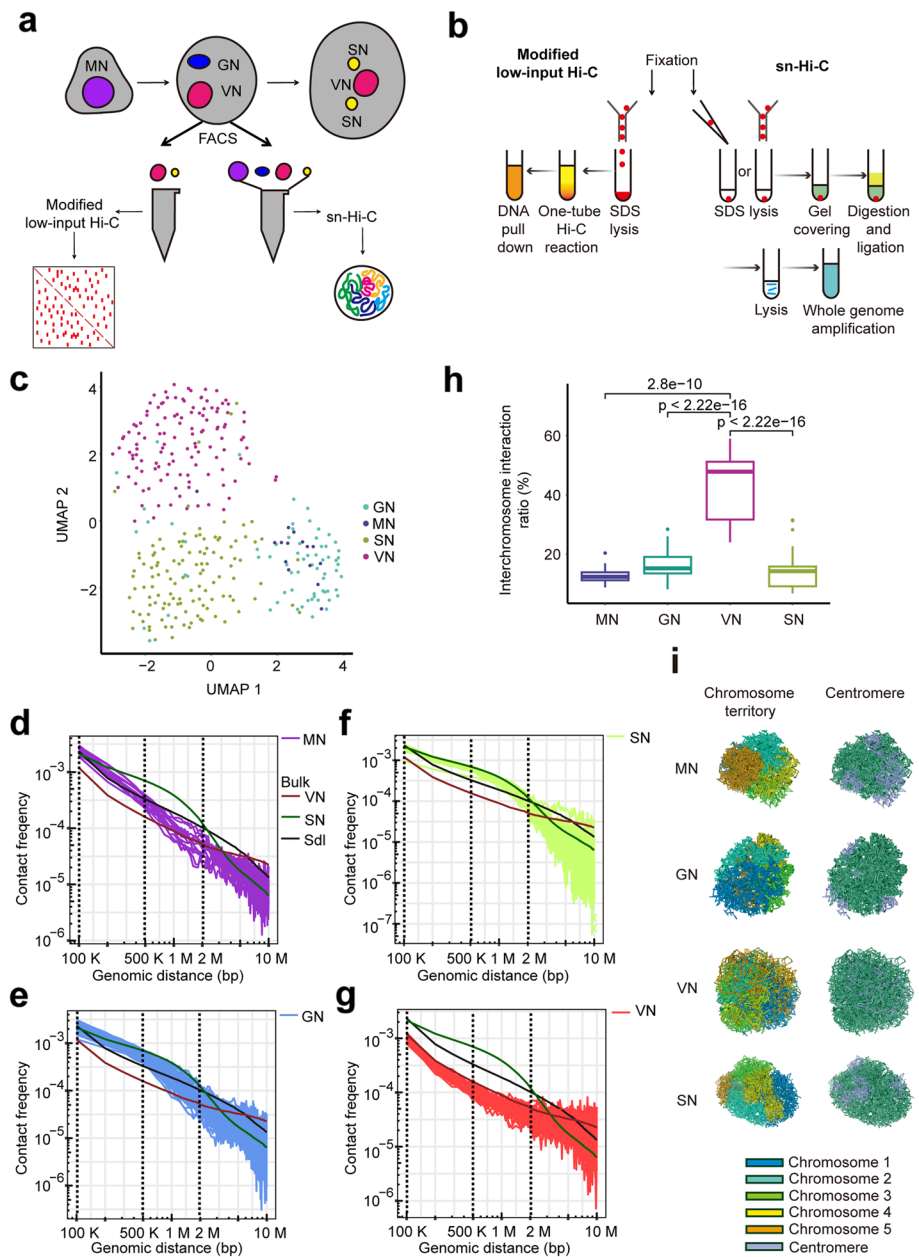


Fig. 1 Chromatin structures in four types of cell nuclei during male gametogenesis. **a** Schematic view of the overall workflow, including the separation of microspores (MN, purple), generative nuclei (GN, blue), sperm nuclei (SN, yellow), and vegetative nuclei (VN, pink), and the sequencing techniques involved in this study. **b** Experimental workflow of modified low-input Hi-C and sn-Hi-C. In brief, the isolated nuclei of male germ cells were subjected to modified low-input Hi-C in one tube or sn-Hi-C with single nuclei covered by gel and subsequent Hi-C. **c** UMAP plot and clustering analysis of the four types of cell nuclei during gametogenesis based on sn-Hi-C data. **d-g** The interaction decay exponent (IDE) curves of microspore nuclei (**d**), generative nuclei (**e**), sperm nuclei (**f**), and vegetative nuclei (**g**), describing the relative contact probability from 100 kb to 10 Mb decay with genomic distance for every single nucleus. In the plots, the IDE curves of seedlings (Sdl), VN and SN for bulk samples are marked in black, dark green, and dark red, respectively. **h** Boxplot of the interchromosome interaction ratio in MN, GN, VN and SN. The border horizontal line and the box represent the median and quartiles, respectively. **i** 3D genome structure of the representative MN, GN, VN, and SN together with centromere distribution. Each color corresponds to one chromatin, and the purple regions represent the centromeres

(Fig. 1c): vegetative nuclei and sperm nuclei were gathered separately, while microspores and generative nuclei were clustered together (Fig. 1c). These results indicate that microspore nuclei and generative nuclei are similar in 3D chromatin structure but differ from vegetative nuclei or sperm nuclei. Interaction decay exponent (IDE) curves profile the features of general chromatin compaction, and those of single-nucleus and bulk samples were finely matched in vegetative and sperm nuclei (Fig. 1d–g). While the short-range interaction could reflect the state of chromatin compaction [37], the genomic distance ranging from 100 kb to 2 Mb has been divided into four intervals to depict the compression. We found no obvious difference in the four cell types ranging from 100 to 200 kb. The contact frequency of generative nuclei and sperm nuclei are higher than microspore nuclei, and the vegetative nuclei have the lowest contact frequency from 200 to 500 kb. (Fig. 1d–f: and Additional File 1: Fig. S5a, b). When focusing the distance from 500 kb to 2 Mb, the contact frequency of sperm nuclei is higher than the counterpart in generative nuclei. These data depicted the compacted process from microspores to sperm (Fig. 1d–f: and Additional File 1: Fig. S5c, d). Consistently, the compactations in generative nuclei varied within a certain range, and the coefficients of variation (CV) of generative nuclei are the highest within the four cell types ranging from 500 kb to 2 Mb, describing the dynamic compaction in generative nuclei (Fig. 1e, f: and Additional File 1: Fig. S6). As the final products of gametogenesis, both sperm nuclei and vegetative nuclei show evident but different changes in comparison with seedling samples. When focusing on the genome distance ranging from 100 kb to 1 Mb, the contact frequencies were higher in sperm nuclei but lower in vegetative nuclei compared to somatic cells. The results indicated that sperm nuclei are more compact, while vegetative nuclei are less compact (Fig. 1f, g). We also calculated the percentage of inter chromosome contacts to quantify the intermingling between different chromosomes, and vegetative nuclei were found to be the most tangled of the four types of cells (Fig. 1h). This can be also observed in the reconstructed models based on the sn-Hi-C data. Microspores, generative nuclei, and sperm nuclei have clear chromosome territories, but vegetative nuclei have intermingled chromatins (Fig. 1i and Additional File 1: Fig. S7). Furthermore, at the single nucleus level, the centromere region of each chromosome exhibits diffusion in vegetative nuclei but remains aggregated in the other cell types (Fig. 1i). Taken together, after the first round of mitosis in microspores, the chromatin tends to maintain clear territories and gradually compacts from the proximal to the distal during the developmental process from generative nuclei to sperm nuclei. Conversely, vegetative nuclei tend to form distinct intermingling chromatin structures.

The different features of higher-order 3D chromatin structure in vegetative and sperm nuclei

Our results demonstrate that vegetative and sperm nuclei have the most specific chromatin structure; therefore, we focused on this structure with bulk samples. In comparison with seedlings, the interchromosome interactions are significantly reduced in sperm nuclei but increased in vegetative nuclei (Fig. 2a), reconfirming that sperm nuclei have clear chromatin territories but vegetative nuclei have intermingled chromatin (Fig. 1h, i). We have mapped the reads from low-input Hi-C data of vegetative nuclei and sperm nuclei to the T2T reference genome (Additional File 1: Fig. S4). We found that

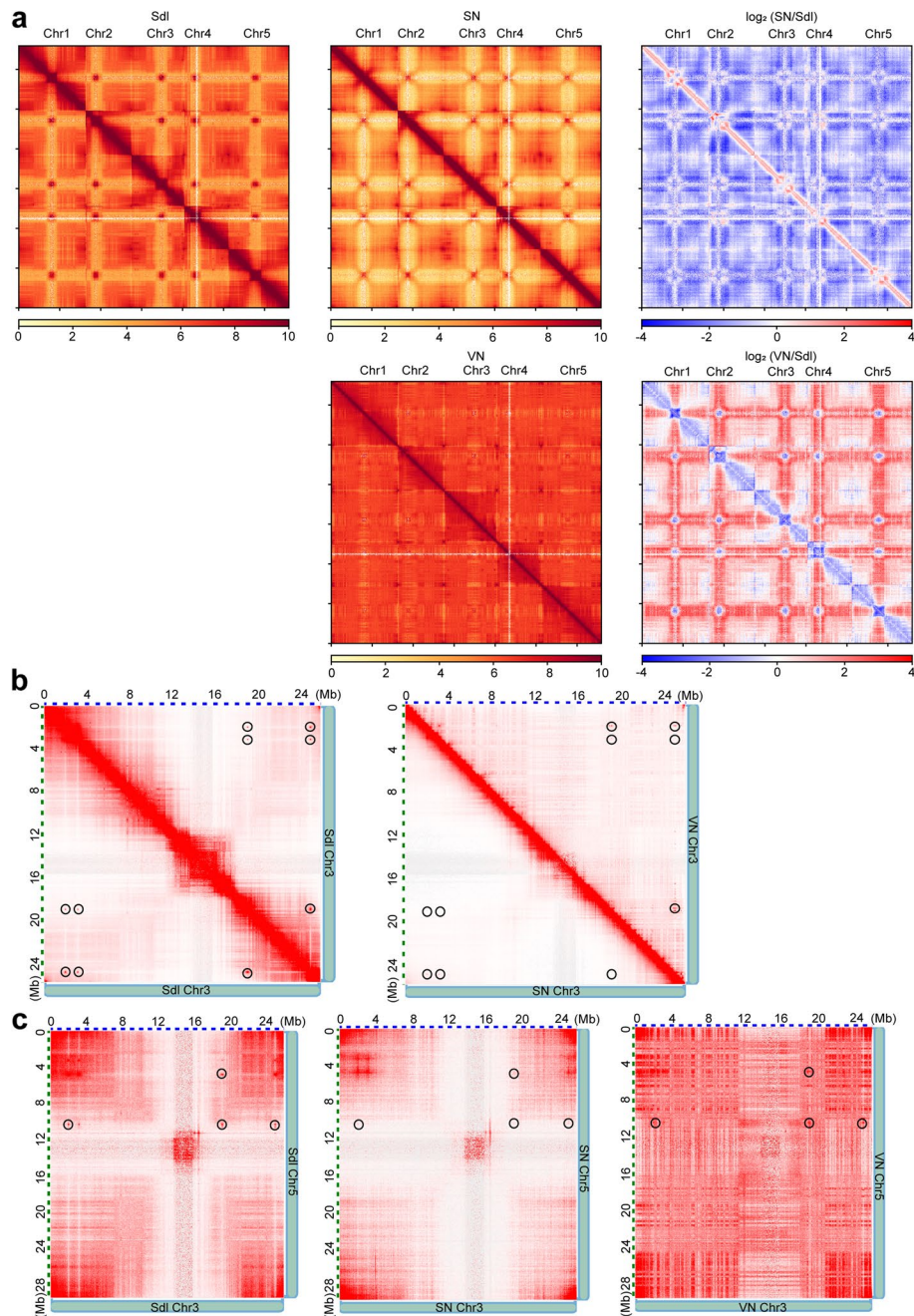


Fig. 2 The intra and interchromosome interactions differ between vegetative and sperm nuclei. **a** The genome-wide Hi-C interaction maps for seedlings, vegetative nuclei (VN), and sperm nuclei (SN). **b, c** Distribution of the *KNOT* structure at chromosome 3 (**b**) or between chromosome 3 and 5 (**c**) in seedlings, sperm nuclei, and vegetative nuclei. The location of *KNOT* structures are marked by black circles

there are no obvious changes of intrachromosome interaction ratio of vegetative nuclei when we aligned the reads to whether TAIR10 genome or Col-CEN, the T2T genome. Notably, the intrachromosome interaction ratio is increased in sperm nuclei when we mapped the reads to the T2T genome. That means when we quantified the interactions of centromere through the new mapping, more intrainteractions, which described the

compact condition, were detected in sperm, but not vegetative nuclei. These results indicate that the centromere regions in sperm nuclei are more aggregated but dispersed in vegetative nuclei which are consistent with our conclusions based on sn-Hi-C data (Fig. 1i). In addition, we found that both the intra- and interchromosome interactions of *KNOT* structures are significantly reduced in sperm nuclei (Fig. 2b, c and Additional File 1: Fig. S8); however, these structures slightly but not significantly decreased in vegetative nuclei (Fig. 2b, c and Additional File 1: Fig. S8). The high degree of chromatin compaction eliminates the long-range interactions within or between chromatins in sperm nuclei (Fig. 1f), resulting in the attenuation of *KNOT* in sperm nuclei (Fig. 2b, c and Additional File 1: Fig. S8). In summary, our results suggest that intermingling chromatin or chromatin compaction is the specific feature in vegetative or sperm nuclei at the chromosome level.

A/B compartments are switched in vegetative or sperm nuclei

The genome is organized into large, self-interacting chromatin compartments, A and B, resulting in plaid patterns in chromatin interaction maps or the derived correlation heatmap [14, 24, 44]. We evaluated whether A/B compartments are still maintained in vegetative and sperm nuclei. In general, A/B compartments are switched in vegetative (34%) or sperm (16%) nuclei compared to that in seedlings (Fig. 3a). Approximately 38 and 13% of A compartments in seedlings are switched to B compartments in vegetative and sperm nuclei, respectively, while roughly 24% of B compartments in seedlings are switched to A compartments in both vegetative and sperm nuclei (Fig. 3a). In *Arabidopsis*, A compartments are located in the chromosome arm region, while B compartments are mainly distributed in the pericentromere or telomeric regions [44]. The global distribution of A/B compartments in sperm nuclei is similar to that in seedlings; however, significantly switched A/B compartments were observed in vegetative nuclei, especially in chromosome arm regions (Fig. 3b and Additional File 1: Fig. S9). Furthermore, we found that the average length of A compartments in vegetative nuclei was significantly shorter than that in seedlings, while the length of B compartments was not significantly changed (Fig. 3c), indicating that A compartments in vegetative nuclei are separated by the newly formed B compartments. In addition, the saddle plots show that the strength of A-A or B-B interactions is weakened in sperm nuclei, but is increased in vegetative nuclei compared that in seedlings (Fig. 3d).

It has been reported that A/B compartments are associated with positive or repressive histone modifications [7, 44, 45]. To further determine whether A/B compartment changes are associated with the changes of histone modification in vegetative or sperm nuclei, we analyzed the relationship between switched regions of A/B compartments and the levels of H3K4me3, H3K9me2, and H3K27me3 [30]. We found that unchanged B compartments and A compartments are enriched with high levels of H3K9me2 or H3K4me3 in both vegetative and sperm nuclei (Fig. 3e, f), suggesting that typical repressive or positive histone modifications contribute to the maintenance of B/A compartments. B to A compartment switching is associated with reduced H3K27me3 levels in both vegetative and sperm nuclei (Fig. 3e, f). H3K27me3 is a repressive modification normally located in chromosome arm regions, which explains why B to A switching was observed in these regions (Fig. 3b). A to B switched regions contain increased H3K9me2

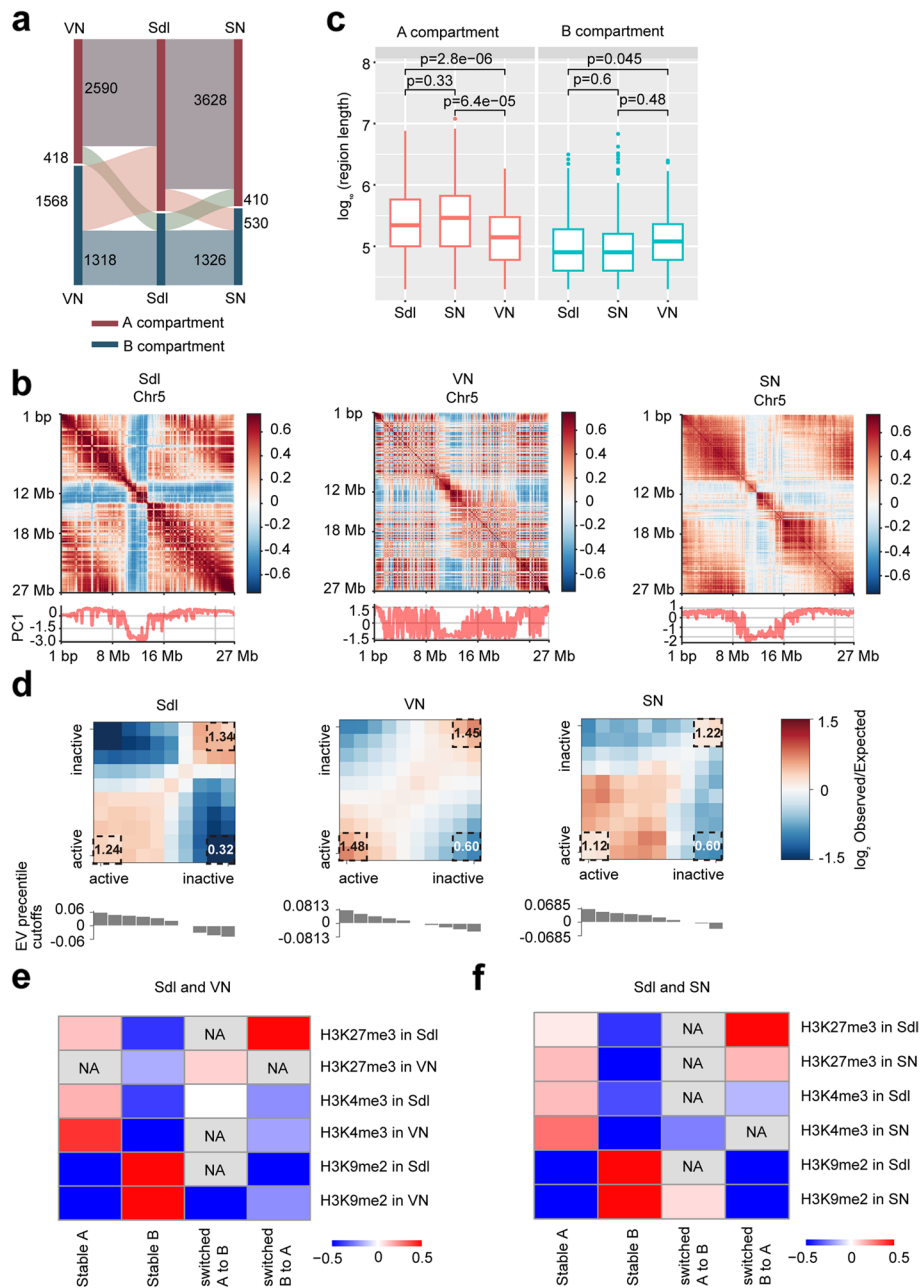


Fig. 3 A/B compartments are switched in vegetative and sperm nuclei. **a** Sankey diagram showing the maintenance or switching of A/B compartments between seedlings and vegetative nuclei or sperm nuclei. **b** The correlation matrix of chromosome 5 in seedlings (left), vegetative nuclei (middle), and sperm nuclei (right). The color bar indicates the relative interaction strength. The lower line plot shows the corresponding PC1 value. **c** Boxplots of the average length of A compartments (left) and B compartments (right) in seedlings, sperm nuclei, and vegetative nuclei. **d** Saddle plots show genome-wide compartmentalization in seedlings, vegetative nuclei, and sperm nuclei. The numbers at the corners of each saddle plot indicate the strength of A-A (bottom left), B-B (top right), and A-B (bottom right) interactions. The eigenvectors under each saddle plot were sorted from largest to smallest, and the intervals were set at 10%. **e, f** Heatmaps show the relative enrichment or depletion (comparing with the randomly selected regions) of histone modifications within the stable or switched A/B compartments between seedlings (Sdl) and vegetative nuclei (e, VN) or sperm nuclei (f, SN). Every row shows the enrichment or depletion of modification in seedlings, vegetative nuclei (e) or sperm nuclei (f). NA means that compared to the randomly selected regions, the modification was not significant ($p > 0.05$) enriched or depleted in stable or switched A/B compartments

and decreased H3K4me3 in sperm nuclei, while increased H3K27me3 in vegetative nuclei (Fig. 3e, f). Taken together, our results demonstrate that changed or maintained typical histone modifications are correlated with compartment switching in vegetative and sperm nuclei.

The switched A/B compartments facilitate vegetative cell-specific function

The switched A/B compartments in vegetative and sperm nuclei led us to further investigate their biological relevance. It has been reported that transposable elements (TEs), located in the pericentromere regions of vegetative nuclei, de-repress and function to reinforce the silencing of TEs in sperm nuclei through the redistribution of siRNAs [46]. We focused on the TEs which are upregulated in vegetative nuclei [47] and examined their spatial position. These TEs were distributed in the pericentromere regions and dispersed throughout vegetative nuclei; by contrast, these TEs were aggregated in sperm nuclei (Fig. 4a). Additionally, the spatial distribution of chromatin compartment structures in vegetative and sperm nuclei was obviously different (Fig. 4a). The B compartments concentrated at the pericentromere regions, and the A compartments distributed at the chromosome arm regions in sperm nucleus; however, the B compartments concentrated at the nuclear periphery and around A compartments in the nuclear center in vegetative nucleus (Fig. 4a), which make the A/B compartment spatial structure similar to that in mammalian nuclei [6]. When we checked the ratio of the differentially

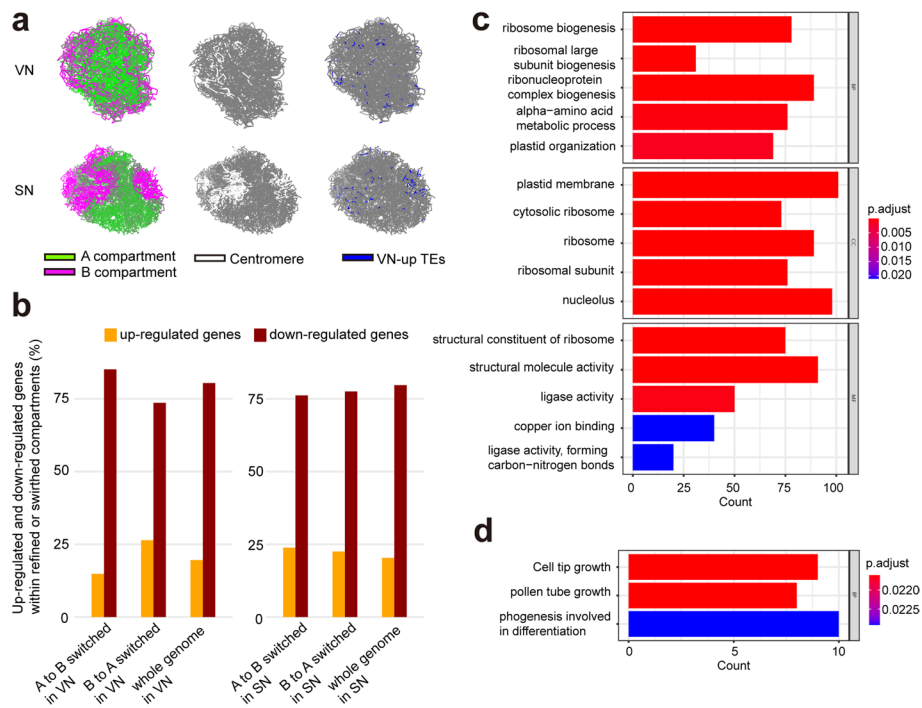


Fig. 4 The switched A/B compartments are positively correlated with mis-regulated genes. **a** Representative 3D structures of vegetative nuclei (VN, top) and sperm nuclei (SN, bottom) show the distribution of A/B compartment (left), centromere (white, middle), and the TEs upregulated in vegetative nuclei (blue, right). **b** The proportion of mis-regulated genes in switched compartments in vegetative nuclei (left) and sperm nuclei (right). **c** GO analysis for the downregulated genes in switched B compartments in vegetative nuclei. **d** GO analysis for the upregulated genes in switched A compartments in vegetative nuclei

expressed genes (DEGs) within switched A/B compartments, we found that there are more upregulated genes within the switched A compartments and downregulated genes within switched B compartments in vegetative nuclei compared to the distribution of DEGs in whole genome compartments (Fig. 4b), which suggests that there is a correlation between switched A/B compartments and gene transcriptional regulation in vegetative nuclei. In contrast, the mis-regulated genes do not show an obvious correlation with the switched A/B compartments in sperm nuclei (Fig. 4b). Moreover, the gene ontology (GO) analysis showed that pollen tube growth-related genes tend to be located at the switched A compartments and upregulated, but the cell development related genes are located at the switched B compartments and repressed in vegetative nuclei (Fig. 4c, d). In summary, these data show that the switched A/B compartments in vegetative nuclei are associated with cell type-specific TE and gene transcriptional regulation.

The active transcriptional center in sperm nuclei facilitates sperm-specific function

It has been reported that although the chromatin is compacted in sperm nuclei, the general transcription is not completely repressed [37]. To investigate where the transcription occurs in compacted sperm nuclei, we divided the simulated single-nucleus structure into three parts by calculating the distances of every particle in the remodeled structure to the mass center and defined the min 25% as the core, the max 25% as the surface, and the remaining parts as the middle. Firstly, we examined the spatial distribution of two typical histone modifications (H3K9me2 and H3K4me3) in sperm nuclei. The surface of sperm nuclei has a higher level of H3K9me2, which decreases gradually toward the middle and core regions. On the other hand, the highest level of H3K4me3 is found in the core of sperm nuclei (Fig. 5a). Accordingly, genes with high transcription are typically located at the core of sperm nuclei (Fig. 5b). Therefore, we defined the core regions in sperm nuclei as the active transcriptional center. Moreover, the genes within the active transcriptional center are involved in meiotic cell cycle regulation (Fig. 5c). It has been reported that the histone variant H2B.8 is involved in the regulation of chromatin compaction in sperm nuclei [37]. To understand whether H2B.8 functions to regulate the active transcriptional center, we used the CRISPR-Cas9 system to generate a *h2b.8* mutant in the *pMGH3::MGH3-eGFP/pACT11::H2B-mRFP* background, which has been described previously (Additional File 1: Fig. S10) [37]. Subsequently, we isolated vegetative and sperm nuclei to perform sn-Hi-C (Additional File 1: Fig. S11). Since H2B.8 is only expressed in sperm but not vegetative nuclei [37], the latter from the *h2b.8* mutant were used as a control. Clustering of vegetative and sperm nuclei in WT and the *h2b.8* mutant based on Hi-C contact maps yielded two clusters (Fig. 5d). Vegetative nuclei from WT or the *h2b.8* mutant mixed together, but sperm nuclei from WT or the *h2b.8* mutant showed difference (Fig. 5e). Next, we reconstructed the 3D genomes of vegetative and sperm nuclei in the *h2b.8* mutant. We found that the inter chromosome interaction ratio is increased in sperm nuclei but not in vegetative nuclei in the *h2b.8* mutant in comparison with that in the WT (Fig. 5e, f), which indicates that H2B.8 compacts chromatin by preventing interchromosome interactions. Although H2B.8 functions to compact chromatin in sperm nucleus [37], the active transcriptional center is maintained in the *h2b.8* mutant sperm nuclei (Fig. 5g). Additionally, the genes within the active transcriptional center significantly overlapped between WT and the *h2b.8* mutant sperm

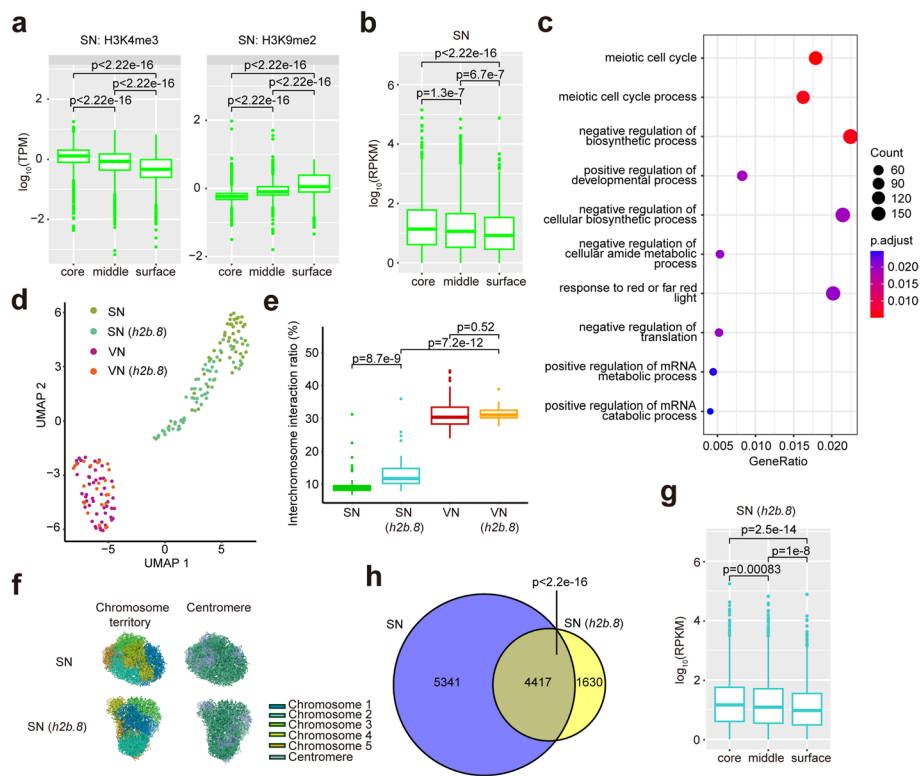


Fig. 5 The active transcriptional center is associated with sperm-specific gene expression. **a** Boxplots indicate the enrichment of H3K4me3 (left) and H3K9me2 (right) in the core, middle, and surface regions of sperm nuclei. **b** Boxplot indicate the transcriptional level in the core, middle, and surface regions of sperm nuclei in WT. **c** GO analysis for genes within core regions in WT sperm nuclei. **d** UMAP plot and clustering analysis of vegetative nuclei (VN) and sperm nuclei (SN) in WT and the *h2b.8* mutant based on sn-Hi-C data. **e** Boxplot shows the interchromosome interaction ratio of vegetative nuclei and sperm nuclei in WT and the *h2b.8* mutant. **f** Reconstructed 3D genome structure of sperm nuclei in WT and the *h2b.8* mutant, with the distribution of five chromosomes and centromeres (the same reconstructed 3D genome structure of sperm nuclei in WT as Fig. 1i). **g** Boxplot indicate the transcriptional level in the core, middle, and surface regions of sperm nuclei in the *h2b.8* mutant. **h** Venn diagram shows overlapped genes within core regions in WT and the *h2b.8* mutant sperm nuclei. *p*-value was calculated by chi-square test

nuclei (Fig. 5h), which may explain why the sperm fertility is not disrupted in the *h2b.8* mutant [37]. Certain core genes in the wild type sperm were redistributed to the middle regions of *h2b.8* mutant sperms, recalling the less compacted but active transcriptional center the *h2b.8* sperm have (Additional File 1: Fig. S12). As a gradually compacted process exists from microspore to sperm (Fig. 1d-f), while the compaction is not necessary for the formation of an active core, we wonder if the active core exists in microspore nuclei and generative nuclei. We have combined the published ATAC-seq and our sn-Hi-C data and found that the chromatin accessibility has decreased from the core region to the surface region in microspore nuclei (Additional File 1: Fig. S13a). Meanwhile, the chromatin accessibility in the surface region of generative nuclei is less than in the core and middle regions (Additional File 1: Fig. S13b). As for vegetative nuclei, the core region, middle region, and surface region have a relatively even state of chromatin accessibility without the structures of either active core or compact silent center (Additional File 1: Fig. S13c). Chromatin accessibility, an indicator of transcription potential [48],

is highly aggregated in the core regions of microspore and generative nuclei but not in vegetative nuclei, indicating the active core is also existent in microspore nuclei and generative nuclei. In summary, these results suggest that the core region in sperm nuclei is an active transcriptional center enriched with H3K4me3, which contributes to sperm-specific transcription pattern maintenance.

Discussion

The previous study which focused on the fertilization in rice isolated 15 cells in total (four eggs, four sperms, four mesophyll cells, and three zygotes) with up to 17,000 effective contacts [5]. We applied FACS and modified sn-Hi-C method to get 324 nuclei in total (15 microspores, 68 generative nuclei, 118 sperm nuclei, and 123 vegetative nuclei) with a median of 41,684 chromatin contacts. Improvement of the FACS and sn-Hi-C method lets us get more nuclei, more contacts and more various and precise cell types, allowing us to better study dynamic changes in 3D chromatin structure during the two rounds of mitosis in plant male gametogenesis. For the common study of the sperm at single nucleus level, there are two similarities between *Arabidopsis* and rice. Firstly, the interchromosomal interaction ratio in sperm was significantly lower than somatic cells in both *Arabidopsis* and rice [5]. Secondly, the compact silent center (CSC) region, a compacted structure which could be analogous with the interactive heterochromatic islands (IHIs) in *Arabidopsis*, appears in egg, zygote and mesophyll cells of rice, but not in sperm [5, 24]. Our data indicates that the *KNOT* structure (formed by IHIs) is also significantly reduced in *Arabidopsis* sperm.

In mammals, 3D chromatin structure reorganized from round spermatid to the mature sperm [25–27], including refined compartments and increased long-range interactions. The general transcription level is significantly low in mature sperm because of the tightly packaged chromatin [39, 49–51]. In *Arabidopsis*, our results profile the progression of male gametogenesis is accompanied by dynamic changes in 3D chromatin structure. The microspore, in which the 3D chromatin structure is similar to that in somatic cells (seedlings), develops towards different structural directions after the first round of mitosis. In vegetative nuclei, chromatin territories become blurred, and the strength of A/B compartments is changed in comparison with those in seedlings, while generative nuclei maintain the chromatin territories and initiate the compaction of chromosomes at the proximal regions. Histone variants H3.10 and H2B.8 are reported to integrate genome in generative and/or sperm nuclei, which are involved in male gametophyte development [36, 37]. Other histone variants may also function in this process to compact chromatin in generative nucleus. Subsequently, two sperm cells are yielded from one generative cell after a second round of mitosis. The compaction of chromatin gradually extends toward the distal regions until complete compaction is reached within the sperm nucleus, which exhibits clear chromatin territories. Moreover, the switched A/B compartments are weakened in comparison with those in seedlings (Fig. 6a). While two directions appeared after the first division and the same direction was kept after the second divide, our results emphasize the relationship between mitosis and cell fate determination in 3D perspective. In addition, the transcription in *Arabidopsis* is maintained at certain level compared to that in mammalian sperm [37–39]. We found that an active transcriptional center with high levels of H3K4me3 maintenance of a relatively

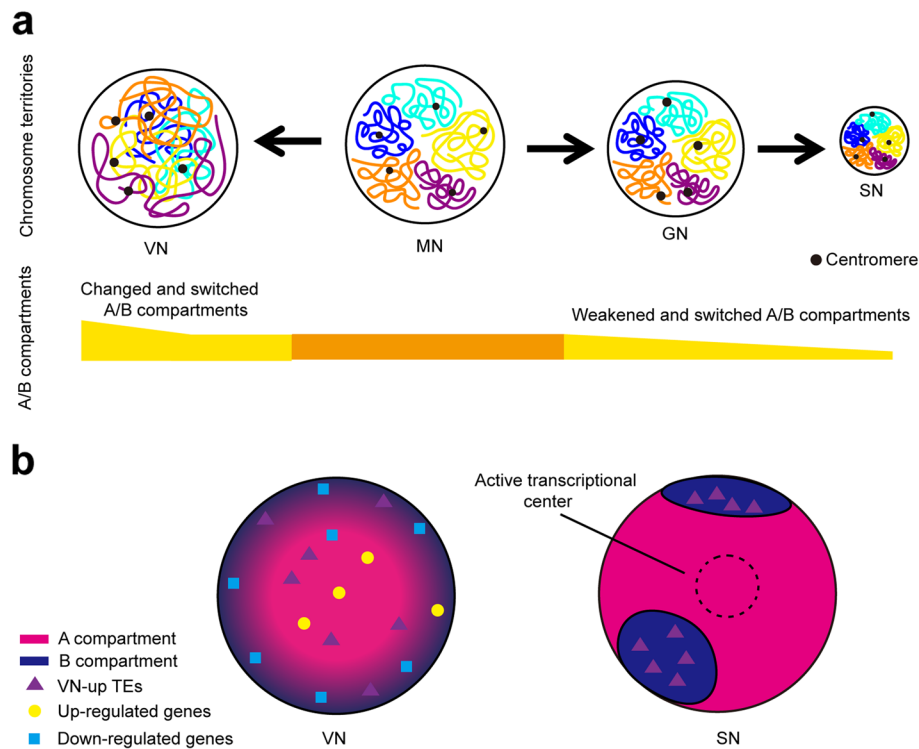


Fig. 6 Schematic model of 3D chromatin organization during two rounds of mitosis of plant male gametogenesis. **a** During the two rounds of mitosis, chromosome territories are clear in microspores (MN), generative nuclei (GN), and sperm nuclei (SN) but lost in vegetative nuclei (VN). The chromosomes in sperm are compact, with weakened/switched A/B compartments, whereas those in vegetative nuclei are intermingled together, strength changed/switched A/B compartments. **b** Transcription of genes and VN-up TEs is closely correlated with switched A/B compartments in vegetative nuclei, the VN-up TEs are distributed in the pericentromeric regions and scattered throughout the whole genome, while transcription is more active in the core region of sperm nuclei, especially that of function-related genes

active transcriptional state of genes related to the meiotic cell cycle regulation (Fig. 6b). Previous paper focused on microscopy analyses in vegetative nuclei and sperm nuclei and conducted bulk Hi-C in seedlings with ectopically express H2B.8 [37]. Our study has confirmed the conclusions about the condensed state of chromatin in sperm nuclei and less compact state of chromatin in vegetative nuclei in previous study [37]. Additionally, our study conducted sn-Hi-C and low input Hi-C in sperm and vegetative nuclei, finely describing the structural formation of the two significant cell types, especially on the A/B compartment switch respective. The Hi-C data in special cell types, but not the ectopic simulating Hi-C, are the true reflection of 3D genome, and give a chance to integrate multiple omics data to describe the structure of sperm and vegetative nuclei and their relationship with transcriptional regulation. Moreover, our data showed that the active transcriptional center is not regulated by H2B.8, which indicates that sperm-specific expression genes are independent of chromatin compaction. The transcription of the sperm-specific genes may contribute to maintaining the active transcriptional center, which is verified by theory [52] that 3D chromatin structure is finally coupled with local transcription. More study would be needed to elucidate how the active transcriptional center maintains in the future.

Vegetative cells are a specific cell type in flowering plants. In comparison with generative cells, vegetative cells undergo certain epigenetic changes such as heterochromatin loss and DNA demethylation, which activate TEs and genes related to pollen function [34, 47, 53]. We observed significant changes in the 3D chromatin structure in vegetative nuclei with the loss of chromosome territories, which is unique compared with other cell types in both animals and plants. It has been found that there is a close relationship between switched A/B compartments and transcriptional regulation during spermatogonial differentiation in mammals [54]. In our study, the correlation between switched A/B compartments and mis-regulated genes in vegetative nuclei is closer than in sperm nuclei, which may correlate with the less compact chromatin structure and blurred chromatin territories. The dramatic switched A/B compartments participate in regulating certain genes such as the pollen tube growth related genes, and may link with changed histone modifications (Fig. 6b). Some studies have mentioned the relationship between A/B compartment switch and the histone modification change. For instance, chromatin remodeling complexes function to regulate switch of A/B compartments through maintaining H3K27me3 [12]. Besides, the loss of linker histone H1 leads to the reduction of H3K27me3 and gain of H3K36me2 which are closely related to the switch of A/B compartments [18]. Furthermore, it has been reported that partial A/B compartments have switched in differentiating spermatogonia in mammals, and several functional genes are related to the switch of A/B compartments [54]. Further studies are needed to investigate the mechanistic insights between histone modifications and genome structures by mutating the writer protein of H3K27me3 or H3K4me3.

Moreover, the vegetative nucleus also can be a special example to explore 3D chromatin structural formation. The fractal globule conformation model is used to explain the formation of chromatin 3D structure in both animals and plants [7, 24]. The chromatin conformation in vegetative nucleus is unique and confirms the other model, equilibrium globule conformation model [7]. Exploring the mechanism of special chromatin formation in vegetative nuclei will help to further understand the equilibrium globule conformation model.

Conclusions

Collectively, our work provides a new blueprint for the dynamics of 3D chromatin structure during the two rounds of mitosis in plant male gametogenesis, which is prominent for the plant reproductive process. We have found that the genome structure of microspore nuclei develops in two distinct directions: vegetative nuclei lose clear chromosome territories and exhibit intermingled chromosomes; the compaction state of chromatin initiates from generative nuclei from the distal regions until the complete compaction state in sperm nuclei. Besides, the nuclei of microspore, generative cell and sperm cell have clear chromosome territories. Furthermore, the 3D chromatin structure has a close relationship with the transcriptional regulation during gametogenesis. The switched A/B compartments in vegetative nuclei are associated with cell type-specific TE and genes related to its function such as pollen tube growth-related genes. Moreover, sperm nuclei exist an active transcriptional center, which is vital for the maintenance of its special transcription pattern. This complete tracking can help to better understand the possible

mechanism of male sterility and provide clues for the construction of sterile lines in crossbreeding.

Methods

Plant materials and growth conditions

Col-0, *pMGH3::MGH3-eGFP/pACT11::H2B-mRFP*, *pHTR10::HTR10-RFP*, and *h2b.8* mutant plants were grown in a Percival growth chamber at 22 °C under long-day (16 h light/8 h dark) conditions.

Construction of the *h2b.8* mutant using CRISPR-Cas9

To create the *h2b.8* mutant, four primers for single-guide RNA (sgRNA) were designed and cloned into the pAtU6-sgRNAs vector [37]. The pAtU6-sgRNA fragment containing the sgRNA sequence was transferred to the $p2 \times 35S$ -Cas9-P2A-GFP-rbcS-E9t and pJim19 vectors, by restrictive enzyme digestion and T4 ligation (for oligonucleotide sequences, see Additional file 3: Table S2). *Agrobacterium tumefaciens* was transformed with the constructs, and the flower-dipping method was used to acquire the transgenic plant in the *pMGH3::MGH3-eGFP/pACT11::H2B-mRFP* background.

Isolation of microspores, generative cell nuclei, vegetative nuclei, and sperm nuclei by FACS

Microspores were isolated by FACS as described previously [40]. Greater than 200,000 microspores were isolated from approximately 3-mL unopened buds. The purity of the microspores was accessed by DAPI staining under the microscope. Then, the microspore cell suspension in $1 \times$ PBS was centrifuged at $2000 \times g$ for 5 min at 4 °C, the supernatant was discarded, and 1 mL $1 \times$ PBS containing a final concentration of 2% formaldehyde solution was added. The sample was fixed for 20 min at room temperature, after which glycine was added at a final concentration of 0.1 M to quench the fixation reaction. The pellets were collected by centrifugation at $2500 \times g$ for 5 min at 4 °C, and the supernatant was discarded. Finally, cells were resuspended in 50 μ L Galbraith Buffer [55] containing 1% Triton™ X-100, 10 mM β -mercaptoethanol, and $1 \times$ complete protease inhibitor cocktail. Microspore cells were lysed by mechanical grinding using a pestle in liquid nitrogen [30]. The intact microspore nuclei were isolated by aspiration using a needle under the microscope.

Generative cell nuclei were isolated from the *pHTR10::HTR10-RFP* marker line [56]. In brief, unopened buds were picked from the marker line and ground in ice-cold 0.3 M mannitol solution. The crude pollen was filtered through a 100- μ m nylon mesh, and Triton™ X-100 was then added at a final concentration of 1%. After centrifugation at $800 \times g$ for 5 min at 4 °C, the supernatant was discarded and the pollen pellet was resuspended in ice-cold Galbraith Buffer [55] containing 1% Triton™ X-100, 10 mM β -mercaptoethanol, and $1 \times$ complete protease inhibitor cocktail [29] and subjected to FACS. The mixture of microspores and bicellular pollen was gated by high-angle scatter (SSC), autofluorescence, and low-angle scatter (FSC) [40]. To further isolate

generative cell nuclei, the mixture of microspores and bicellular pollen was collected by centrifugation at $2500 \times g$ for 5 min at 4 °C. The supernatant was then discarded and the pellet was resuspended in 3 volumes of Buffer A [57]. A beating protocol with 500- μ m glass beads was run for 90 s at 30 Hz [57], and the suspension was subjected to FACS. The generative cell nuclei were isolated based on the RFP signal.

Dry pollen was harvested from the *pMGH3::MGH3-eGFP/pACT11::H2B-mRFP* marker line, and sperm and vegetative nuclei were isolated by FACS as described previously [40]. Greater than 30,000 sperm nuclei and vegetative nuclei were isolated from approximately 5-mL open flowers.

Zeiss LSM 900 Airyscan laser confocal microscopy has been used to detect GFP or RFP fluorescence signals, and the obtained images were processed by using ZEN Microscopy software.

Sample pre-processing

Samples used for the analysis of nuclei from sperm, vegetative, or generative cells were centrifuged at $1300 \times g$ for 5 min at 4 °C. The supernatant was discarded, the pellets were resuspended in 500 μ L 1 \times PBS, and the samples were centrifuged again. Nuclei were collected in 500 μ L 1 \times PBS containing 75 μ L 16% PFA (Thermo Fisher 28,906), fixed at room temperature for 20 min with rotation, and then quenched with 50 μ L 2% BSA (NEB B9000S). The supernatant was removed after centrifugation at $2000 \times g$ for 5 min, and the pellets were resuspended in 1 mL 1 \times PBS and then subjected to FACS. Nuclei were sorted in the single-cell or 4-way mode, depending on the subsequent experiment, using a BD FACSAria™ Cell Sorter (65,011,040). Briefly, sperm nuclei were sorted by FITC, and vegetative and generative nuclei were sorted by Texas Red.

Single-nucleus Hi-C on agarose

The protocol was used for the single-cell Hi-C experiments [6, 13, 58]. Microspore, sperm, vegetative, and generative nuclei were sorted into 200- μ L tubes containing 2.5 μ L 0.3% SDS buffer in NEBuffer r3.1 (B6003S, NEB). After gentle centrifugation, the mixture was incubated at 37 °C for 1 h, and then quenched with a solution containing 1 μ L Triton™ X-100, 0.125 μ L water, and 0.125 μ L NEBuffer r3.1 at 37 °C for 15 min. The solution was set with 1.25 μ L 2% low-melting point agarose (16,520,050, ThermoFisher) cooled at 4 °C for 10 min. The subsequent incubations and washes were carried out by altering the upper buffer of the gel. Nuclei were digested at 37 °C overnight with 0.3 μ L Dpn II (R0543M, NEB) in 1 \times NEBuffer r3.1, and then washed twice with T4 ligation buffer containing 0.1 mg/mL BSA. Ligation was performed at 16 °C for 12 h using 0.1 μ L 400 U/ μ L T4 ligase (M0202L, NEB) in a total volume of 10 μ L 1 \times T4 Ligation Buffer containing 0.1 mg/mL BSA.

After washing twice with Reverse-crosslinking Buffer (50 mM NaCl, 20 mM Tris pH 8.0, 0.15% Triton™ X-100, 1 mM EDTA, 25 mM DTT), the gel was melted at 65 °C for 5 min, and then 1 μ L 6 mg/mL Qiagen Protease (QIAGEN 19157) was added. Nuclei were lysed at 50 °C for 3 h and then at 70 °C for 1 h. The amplification was performed by adding 34 μ L Amplification Mixture (4 μ L 10 \times ThermoPol buffer, 1.2 μ L 10 mM dNTP, 0.6 μ L 50 μ M GAT5 primer, 0.6 μ L 50 μ M GAT5-7N primer, 0.3 μ L 100 mM MgSO₄,

1 μL Deep Vent (exo-) (NEB M0259L), and 26.3 μL water) and incubating under the following program: 95 $^{\circ}\text{C} \times 5$ min; 4 $^{\circ}\text{C} \times 50$ s, 10 $^{\circ}\text{C} \times 50$ s, 20 $^{\circ}\text{C} \times 50$ s, 30 $^{\circ}\text{C} \times 50$ s, 40 $^{\circ}\text{C} \times 45$ s, 50 $^{\circ}\text{C} \times 45$ s, 65 $^{\circ}\text{C} \times 4$ min, 95 $^{\circ}\text{C} \times 20$ s, 58 $^{\circ}\text{C} \times 20$ s for a total of 10 cycles; 95 $^{\circ}\text{C} \times 1$ min; 95 $^{\circ}\text{C} \times 20$ s, 58 $^{\circ}\text{C} \times 30$ s, 72 $^{\circ}\text{C} \times 3$ min for a total of 14 cycles; 72 $^{\circ}\text{C} \times 5$ min and hold at 4 $^{\circ}\text{C}$.

Library construction and sequencing

The single-cell pre-amplification product was diluted according to the average concentration to 5 ng/ μL and 2 μL each diluted sample was transposed by the addition of 3 μL Transposition Mixture (1 μL 5X TTBL, 0.25 μL TTE Mix V50 (Vayme TD501) 1.75 μL water) and incubated at 55 $^{\circ}\text{C}$ for 10 min. Transposition was stopped by adding 1.25 μL 0.2% SDS, and then the plate was incubated at room temperature for 10 min. A 2- μL aliquot of 5 μM i5 index, 2 μL 5 μM i7 index, and 11.55 μL PCR mixture (4 μL 5 \times KAPA HiFi GC Buffer, 0.6 μL 10 mM dNTP, 0.4 μL KAPA HiFi DNA Polymerase (KAPA KK2102), and 6.55 μL water) were added and incubated under the following program: (1) 72 $^{\circ}\text{C} \times 3$ min; (2) 98 $^{\circ}\text{C} \times 30$ s; (3) 98 $^{\circ}\text{C} \times 15$ s; (4) 60 $^{\circ}\text{C} \times 30$ s; (5) 72 $^{\circ}\text{C}$ 2 min, with steps 3–5 cycled 11 times; (6) 72 $^{\circ}\text{C} \times 5$ min; (7) hold at 4 $^{\circ}\text{C}$. The barcoded libraries were pooled and then sized using 0.6X and 0.15X AMPure XP Beads (Beckman. A63881). The final libraries were sequenced with paired-end 150-bp reads on a T7 platform according to the manufacturer's instructions. To obtain a well-modeled structure with sufficient contacts, 0.3 Gb data for each cell were adopted to reach a near-saturated contact number.

Modified low-input Hi-C

The method was modified from a previously described low-input Hi-C for mammalian tissues [20, 59, 60]. Briefly, the nuclei of generative, vegetative, and sperm cells were collected by FACS and centrifuged at 2500 $\times g$ for 5 min to remove the supernatant; 5 μL liquid was left. A 5 μL aliquot of 1% SDS in 1 \times NEBuffer 2 was then added, mixed, and incubated at 61 $^{\circ}\text{C}$ for 10 min. Subsequently, 20 μL 3% TritonTM X-100 was added, vortexed slightly, and allowed to react at 37 $^{\circ}\text{C}$ for 15 min. Digestion was carried out using 2 μL MboI (R0147M, NEB) at 37 $^{\circ}\text{C}$ overnight, followed by inactivation for 20 min at 62 $^{\circ}\text{C}$. Then gap-filling mixture (0.45 μL 10 mM dCTP/dGTP/dTTP mixture, 3.75 μL 0.4 mM Biotin-14-dATP (19,524,016, invitrogen), and 2 μL 5 U/ μL Klenow (M0210L, NEB)) was added and incubated at 37 $^{\circ}\text{C}$ for 90 min. Ligation was performed using 80 μL mixture (12 μL 10 \times Ligation Buffer, 7 μL 10% TritonTM X-100, 0.6 μL 2% BSA, 1 μL 400 U/ μL T4 Ligase, and 59.4 μL water) for 4 h at 16 $^{\circ}\text{C}$. Cells were lysed in 5 μL 60 mg/mL Qiagen Protease and 1 μL 5 M NaCl for 3 h at 50 $^{\circ}\text{C}$, and then the reaction was stopped at 70 $^{\circ}\text{C}$ for 30 min. The lysate was purified using a Zymo DNA purification kit by sequential elution with 6 μL water 2–3 times at 50 $^{\circ}\text{C}$.

Library construction Tagmentation was carried out by Tn5 insertion (TD502, Vazyme). Eluted DNA was added to 6 μL TTBL buffer and X μL TTE (X is the amount of DNA in ng). A total of 30 μL solution was de-acted at 55 $^{\circ}\text{C}$ for 10 min. A 5- μL aliquot of TS buffer was added and incubated for 10 min to stop the reaction. Next, 10 μL 5 \times TAB, 4 μL water, and 1 μL TAE was added for elongation at 72 $^{\circ}\text{C}$ for 3 min. The mixture was then transferred to a tube containing washed MyOne Streptavidin C1 (35002D,

ThermoFisher) beads in 50 μ L 2 \times B&W buffer. After incubation for 15 min with rotation, the beads were washed twice with 80 μ L 1 \times B&W buffer by shaking for 2 min at 55 $^{\circ}$ C. The beads were buffered with 27.5 μ L water and transferred to a fresh tube. Subsequently, 10 μ L 5 \times HiFi GC buffer, 1.5 μ L 10 mM dNTP, 1 μ L KAPA, and 5 μ L 5 mM bar-coded i5/i7 primers were mixed together and incubated under the following program: (1) 72 $^{\circ}$ C \times 3 min; (2) 98 $^{\circ}$ C \times 30 s; (3) 98 $^{\circ}$ C \times 15 s; (4) 60 $^{\circ}$ C \times 30 s; (5) 72 $^{\circ}$ C \times 2 min, with 3–5 steps cycled 10–13 times; (6) 72 $^{\circ}$ C 5 min; (7) hold at 4 $^{\circ}$ C.

The pooled sample was directly sized with 0.75X AMPure XP Beads (Beckman. A63881). The final libraries were sequenced with paired-end 150-bp reads on a T7 platform according to the manufacturer's instructions. To obtain a fine resolution with clear high-order structures, each sample was sequenced with 50–100 Gb data according to the sample size.

Analysis of single-nucleus Hi-C data

The sn-Hi-C data were preprocessed as previously reported [6]. The sequence reads were mapped to the TAIR10 reference genome using BWA-mem2 in 5SP mode. The reads were then aligned pairwise, and contacts were generated using hickit with defined parameters. We skipped contact phasing and cleaning processes in all cells due to the haploid nature and lack of SNPs. For quality control, cells with $< 10,000$ contacts were excluded. scHiCluster [61] and Seurat [62] were used for dimensionality reduction and clustering under default parameters. The first 100 singular values for scHiCluster were used in Seurat to “RunPCA,” “FindNeighbours,” “FindClusters,” and “RunUMAP”. Hickit was used to generate the reconstructed 3D structure of each cell. The parameters were set as -r1M -c1 -r10m -c2 to filter the interactions, and the 3D structure was reconstructed gradually at higher resolution in the order of 4 Mb, 1 Mb, 200 kb, 50 kb, 20 kb, and 5 kb. “dip-c/scripts/hickit_3dg_to_3dg_rescale_unit.sh” and “dip-c align” were used to rescale the backbone distance of each reconstructed structure to 1.0 particle radii and estimate the uncertainty of the 3D structures, respectively. The structures were analyzed using “dip-c color -C” [6] to identify their surface and core regions. The distance from the simulated center in each single nucleus has been calculated, then the average distance of each particle in different genome structures is calculated as the final distance of this particle. The 5-kb particles were arranged according to their distance from the central mass of the reconstructed structure, with the minimum 25% of the final average distance was defined as the core region. PyMOL was used for data visualization, adjusting the diameter of the ball and stick structure according to the characteristics of each structure to clearly show the structure.

Analysis of bulk Hi-C data

After the data were filtered using fatSP [63], the interaction matrix was processed by HiC-Pro [64], and the converted matrix was previewed using Juicebox [65] to show the interactions. The bulk Hi-C data were mapped to the TAIR 10 and the Col-CEN genome [66]. For the 100 kb resolution matrix, after correcting the differences in sequencing depth between samples using HiCExplorers [67], especially by hicNormalize and hicCorrectMatrix, hicPlotDistVsCounts were used to investigate the variation in chromatin interaction frequency with distance. From 100 kb to 2 Mb, the distance ranges were

separated into four intervals, and the contact frequency in each interval was summed and compared between different cell types. The coefficient of variation was calculated by taking the standard deviation and dividing it by the mean. HOMER [68] was used to compute the feature vector and define the chromatin compartments, at a resolution of 20 kb and a sliding window of 60 kb, and then correct for the activation-modified region of H3K4me3. FAN-C [69] was used to determine the intensity of chromatin compartmentalization. The feature vectors were calculated at a resolution of 40 kb; the feature vectors were sorted from largest to smallest; the most active A compartment to the most inhibited B compartment was defined at 10% intervals; and the observed/expected values for the interactions within and between these percentile intervals were calculated and displayed. HiCPlotter [70], Intervene [71], and Seqplot [72] were used for data visualization.

Supplementary Information

The online version contains supplementary material available at <https://doi.org/10.1186/s13059-025-03496-8>.

Additional file 1. Supplementary figures S1-S13.

Additional file 2. Table S1. List of sn-Hi-C results.

Additional file 3. Table S2. List of primers used in the present study.

Additional file 4. Table S3. Summary of the public datasets used in the present study.

Additional file 5. Review history.

Acknowledgements

We thank Drs. Lijia Qu and Sheng Zhong (Peking University) for providing the seeds of the *pHTR10::HTR10-RFP* marker line, Jörg D Becker (Universidade Nova de Lisboa) for providing the seeds of the *pMGH3::MGH3-eGFP/pACT11::H2B-mRFP* marker line. We appreciate Dr. Quanle Xu and Ms. Ruihong Qu (Northwest A&F University) for providing technical support. Special thanks are extended to Dr. Genji Qin (Peking University) for putting considerable time and effort into their comments on the manuscript. The present study was carried out at the Peking University High Performance Computing Platform, and the calculations were performed on CLS-HPC.

Review history

The review history is available as Additional file 5.

Peer review information

Wenjing She was the primary editor of this article and managed its editorial process and peer review in collaboration with the rest of the editorial team.

Authors' contributions

Y.Z. conceived the research. Z.S., Q.X., T.Y., Y.L., J.S., Z.L., Y.C., H.X., X.Y., and H.Z. conducted the experiments. M.Y., D.W., H.H., X.Y., Y.J., X.W.D., and D.X. analyzed the data. Z.S., Q.X., M.Y., and Y.Z. wrote the manuscript. All authors read and approved the final manuscript.

Funding

This work was supported by Biological Breeding-National Science and Technology Major Project (2023ZD04073); grants 32370612 (Yue Zhou), and 32300463 (Tingting Yang) from the National Natural Science Foundation of China; grant JCTD-2022-06 (Yue Zhou) supported by CAS Youth Interdisciplinary Team; grant 8206300743 and GZC20230083 (Tingting Yang) from China Postdoctoral Science Foundation; startup funds from the State Key Laboratory of Gene Function and Modulation Research, the School of Advanced Agricultural Sciences, and the Peking-Tsinghua Center for Life Sciences at Peking University (Yue Zhou); startup funds (Dong Xing) from the Beijing Advanced Innovation Center for Genomics (ICG).

Data availability

For published RNA-seq data, the filtered read segments were mapped to the *Arabidopsis* TAIR 10 reference genome using HISAT2 [73], and the results were sorted, indexed, and compressed using SAMtools [74]. StringTie [75] was used for transcription quantitation. DEseq2 [76] was used to identify differentially expressed genes. bamCoverage in deepTools [77] was used to average read segment coverage for the generation of Bigwig files. For ChIP-seq and ATAC-seq data, Bowtie2 [78] was used to map the genome; Picard marked repeated read segments generated by PCR; and bamCoverage [77] generated Bigwig files. Bedmap [79] and multiBigwigSummary [77] were used to visualize or count the modification or expression levels in certain regions or bins. All sequencing data generated in the present study have been deposited into the European Nucleotide Archive (ENA) under the accession number: PRJEB71351 [80]. All the published datasets [81–85] and their relevant papers [11, 29, 30, 37] used in present study are listed in Additional file 4: Table S3.

Declarations

Ethics approval and consent to participate

Not applicable.

Consent for publication

Not applicable.

Competing interests

The authors declare that they have no competing interests.

Received: 15 March 2024 Accepted: 5 February 2025

Published online: 10 February 2025

References

- Kempfer R, Pombo A. Methods for mapping 3D chromosome architecture. *Nat Rev Genet.* 2020;21:207–26.
- Mohanta TK, Mishra AK, Al-Harrasi A. The 3D Genome: From Structure to Function. *Int J Mol Sci.* 2021;22:11585.
- Smallwood A, Ren B. Genome organization and long-range regulation of gene expression by enhancers. *Curr Opin Cell Biol.* 2013;25:387–94.
- Sexton T, Yaffe E, Kenigsberg E, Bantignies F, Leblanc B, Hoichman M, Parrinello H, Tanay A, Cavalli G. Three-dimensional folding and functional organization principles of the *Drosophila* genome. *Cell.* 2012;148:458–72.
- Zhou S, Jiang W, Zhao Y, Zhou DX. Single-cell three-dimensional genome structures of rice gametes and unicellular zygotes. *Nat Plants.* 2019;5:795–800.
- Tan L, Xing D, Chang CH, Li H, Xie XS. Three-dimensional genome structures of single diploid human cells. *Science.* 2018;361:924–8.
- Lieberman-Aiden E, van Berkum NL, Williams L, Imakaev M, Ragozcy T, Telling A, Amit I, Lajoie BR, Sabo PJ, Dorschner MO, et al. Comprehensive mapping of long-range interactions reveals folding principles of the human genome. *Science.* 2009;326:289–93.
- Ricci WA, Lu Z, Ji L, Marand AP, Ethridge CL, Murphy NG, Noshay JM, Galli M, Mejía-Guerra MK, Colomé-Tatché M, et al. Widespread long-range cis-regulatory elements in the maize genome. *Nat Plants.* 2019;5:1237–49.
- Feng S, Cokus SJ, Schubert V, Zhai J, Pellegrini M, Jacobsen SE. Genome-wide Hi-C analyses in wild-type and mutants reveal high-resolution chromatin interactions in *Arabidopsis*. *Mol Cell.* 2014;55:694–707.
- Wang M, Wang P, Lin M, Ye Z, Li G, Tu L, Shen C, Li J, Yang Q, Zhang X. Evolutionary dynamics of 3D genome architecture following polyploidization in cotton. *Nat Plants.* 2018;4:90–7.
- Yin X, Romero-Campero FJ, Yang M, Baile F, Cao Y, Shu J, Luo L, Wang D, Sun S, Yan P, et al. Binding by the Polycomb complex component BMI1 and H2A monoubiquitination shape local and long-range interactions in the *Arabidopsis* genome. *Plant Cell.* 2023;35:2484–503.
- Yang T, Wang D, Tian G, Sun L, Yang M, Yin X, Xiao J, Sheng Y, Zhu D, He H, Zhou Y. Chromatin remodeling complexes regulate genome architecture in *Arabidopsis*. *Plant Cell.* 2022;34:2638–51.
- Flyamer IM, Gassler J, Imakaev M, Brandão HB, Ulianov SV, Abdennur N, Razin SV, Mirny LA, Tachibana-Konwalski K. Single-nucleus Hi-C reveals unique chromatin reorganization at oocyte-to-zygote transition. *Nature.* 2017;544:110–4.
- Liu C, Cheng YJ, Wang JW, Weigel D. Prominent topologically associated domains differentiate global chromatin packing in rice from *Arabidopsis*. *Nat Plants.* 2017;3:742–8.
- Stevens TJ, Lando D, Basu S, Atkinson LP, Cao Y, Lee SF, Leeb M, Wohlfahrt KJ, Boucher W, O’Shaughnessy-Kirwan A, et al. 3D structures of individual mammalian genomes studied by single-cell Hi-C. *Nature.* 2017;544:59–64.
- Hoencamp C, Dudchenko O, Elbatsh AMO, Brahmachari S, Raaijmakers JA, van Schaik T, Sedeño Cacciatore A, Contessoto VG, van Heesbeen R, van den Broek B, et al. 3D genomics across the tree of life reveals condensin II as a determinant of architecture type. *Science.* 2021;372:984–9.
- Willcockson MA, Heaton SE, Weiss CN, Bartholdy BA, Botbol Y, Mishra LN, Sidhwani DS, Wilson TJ, Pinto HB, Maron MI, et al. H1 histones control the epigenetic landscape by local chromatin compaction. *Nature.* 2021;589:293–8.
- Yusufova N, Kloetgen A, Teater M, Osunsade A, Camarillo JM, Chin CR, Doane AS, Venters BJ, Portillo-Ledesma S, Conway J, et al. Histone H1 loss drives lymphoma by disrupting 3D chromatin architecture. *Nature.* 2021;589:299–305.
- He S, Yu Y, Wang L, Zhang J, Bai Z, Li G, Li P, Feng X. Linker histone H1 drives heterochromatin condensation via phase separation in *Arabidopsis*. *Plant Cell.* 2024;36:1829–43.
- Ke Y, Xu Y, Chen X, Feng S, Liu Z, Sun Y, Yao X, Li F, Zhu W, Gao L, et al. 3D Chromatin Structures of Mature Gametes and Structural Reprogramming during Mammalian Embryogenesis. *Cell.* 2017;170:367–81.
- Phillips JE, Corces VG. CTCF: Master Weaver of the Genome. *Cell.* 2009;137:1194–211.
- Szabo Q, Bantignies F, Cavalli G. Principles of genome folding into topologically associating domains. *Sci Adv.* 2019;5:eaaw1668.
- Karaaslan ES, Wang N, Faiss N, Liang Y, Montgomery SA, Laubinger S, Berendzen KW, Berger F, Breuninger H, Liu C. Marchantia TCP transcription factor activity correlates with three-dimensional chromatin structure. *Nat Plants.* 2020;6:1250–61.
- Grob S, Schmid MW, Grossniklaus U. Hi-C Analysis in *Arabidopsis* Identifies the KNOT, a Structure with Similarities to the flamenco Locus of *Drosophila*. *Mol Cell.* 2014;55:678–93.
- Hao SL, Ni FD, Yang WX. The dynamics and regulation of chromatin remodeling during spermiogenesis. *Gene.* 2019;706:201–10.
- Bryant JM, Meyer-Ficca ML, Dang VM, Berger SL, Meyer RG. Separation of spermatogenic cell types using STA-PUT velocity sedimentation. *J Vis Exp.* 2013;9:50648.

27. Wang Y, Wang H, Zhang Y, Du Z, Si W, Fan S, Qin D, Wang M, Duan Y, Li L, et al. Reprogramming of Meiotic Chromatin Architecture during Spermatogenesis. *Mol Cell*. 2019;73:547–61.
28. Huang J, Dong J, Qu LJ. From birth to function: Male gametophyte development in flowering plants. *Curr Opin Plant Biol*. 2021;63: 102118.
29. Borg M, Papareddy RK, Dombey R, Axelsson E, Nodine MD, Twell D, Berger F. Epigenetic reprogramming rewires transcription during the alternation of generations in *Arabidopsis*. *Elife*. 2021;10: e61894.
30. Zhu D, Wen Y, Yao W, Zheng H, Zhou S, Zhang Q, Qu LJ, Chen X, Wu Z. Distinct chromatin signatures in the *Arabidopsis* male gametophyte. *Nat Genet*. 2023;55:706–20.
31. Long J, Walker J, She W, Aldridge B, Gao H, Deans S, Vickers M, Feng X. Nurse cell-derived small RNAs define paternal epigenetic inheritance in *Arabidopsis*. *Science*. 2021;373:eabh0556.
32. Ikeda Y, Nishihama R, Yamaoka S, Arteaga-Vazquez MA, Aguilar-Cruz A, Grimanelli D, Pogorelnik R, Martienssen RA, Yamato K, Kohchi T, et al. Loss of CG Methylation in *Marchantia polymorpha* Causes Disorganization of Cell Division and Reveals Unique DNA Methylation Regulatory Mechanisms of Non-CG Methylation. *Plant Cell Physiol*. 2018;59:2421–31.
33. Hajkova P. Epigenetic reprogramming in the germline: towards the ground state of the epigenome. *Philos Trans R Soc Lond B Biol Sci*. 2011;366:2266–73.
34. Schoft VK, Chumak N, Choi Y, Hannon M, Garcia-Aguilar M, Machlicova A, Slusarz L, Mosiolek M, Park JS, Park GT, et al. Function of the DEMETER DNA glycosylase in the *Arabidopsis thaliana* male gametophyte. *Proc Natl Acad Sci U S A*. 2011;108:8042–7.
35. Huang X, Sun MX. H3K27 methylation regulates the fate of two cell lineages in male gametophytes. *Plant Cell*. 2022;34:2989–3005.
36. Borg M, Jacob Y, Susaki D, LeBlanc C, Buendía D, Axelsson E, Kawashima T, Voigt P, Boavida L, Becker J, et al. Targeted reprogramming of H3K27me3 resets epigenetic memory in plant paternal chromatin. *Nat Cell Biol*. 2020;22:621–9.
37. Buttress T, He S, Wang L, Zhou S, Saalbach G, Vickers M, Li G, Li P, Feng X. Histone H2B.8 compacts flowering plant sperm through chromatin phase separation. *Nature*. 2022;611:614–622.
38. Pandupuspitasari NS, Khan FA, Huang C, Ali A, Yousaf MR, Shakeel F, Putri EM, Negara W, Muktiani A, Prasetiyono B, et al. Recent advances in chromosome capture techniques unraveling 3D genome architecture in germ cells, health, and disease. *Funct Integr Genomics*. 2023;23:214.
39. Battulin N, Fishman VS, Mazur AM, Pomaznoy M, Khabarova AA, Afonnikov DA, Prokhortchouk EB, Serov OL. Comparison of the three-dimensional organization of sperm and fibroblast genomes using the Hi-C approach. *Genome Biol*. 2015;16:77.
40. Borges F, Gardner R, Lopes T, Calarco JP, Boavida LC, Slotkin RK, Martienssen RA, Becker JD. FACS-based purification of *Arabidopsis* microspores, sperm cells and vegetative nuclei. *Plant Methods*. 2012;8:44.
41. Lando D, Basu S, Stevens TJ, Riddell A, Wohlfahrt KJ, Cao Y, Boucher W, Leeb M, Atkinson LP, Lee SF, et al. Combining fluorescence imaging with Hi-C to study 3D genome architecture of the same single cell. *Nat Protoc*. 2018;13:1034–61.
42. Wang C, Liu C, Roqueiro D, Grimm D, Schwab R, Becker C, Lanz C, Weigel D. Genome-wide analysis of local chromatin packing in *Arabidopsis thaliana*. *Genome Res*. 2015;25:246–56.
43. Liu C, Wang C, Wang G, Becker C, Zaidem M, Weigel D. Genome-wide analysis of chromatin packing in *Arabidopsis thaliana* at single-gene resolution. *Genome Res*. 2016;26:1057–68.
44. Dogan ES, Liu C. Three-dimensional chromatin packing and positioning of plant genomes. *Nat Plants*. 2018;4:521–9.
45. Sexton T, Cavalli G. The role of chromosome domains in shaping the functional genome. *Cell*. 2015;160:1049–59.
46. Slotkin RK, Vaughn M, Borges F, Tanurdzic M, Becker JD, Feijó JA, Martienssen RA. Epigenetic reprogramming and small RNA silencing of transposable elements in pollen. *Cell*. 2009;136:461–72.
47. He S, Vickers M, Zhang J, Feng X. Natural depletion of histone H1 in sex cells causes DNA demethylation, heterochromatin decondensation and transposon activation. *Elife*. 2019;8: e42530.
48. Grandi FC, Modi H, Kampman L, Corces MR. Chromatin accessibility profiling by ATAC-seq. *Nat Protoc*. 2022;17:1518–52.
49. Okada Y. Sperm chromatin structure: Insights from in vitro to in situ experiments. *Curr Opin Cell Biol*. 2022;75: 102075.
50. Rathke C, Baarends WM, Awe S, Renkawitz-Pohl R. Chromatin dynamics during spermiogenesis. *Biochim Biophys Acta*. 2014;1839:155–68.
51. Jung YH, Sauria MEG, Lyu X, Cheema MS, Ausio J, Taylor J, Corces VG. Chromatin States in Mouse Sperm Correlate with Embryonic and Adult Regulatory Landscapes. *Cell Rep*. 2017;18:1366–82.
52. Stadhouders R, Filion GJ, Graf T. Transcription factors and 3D genome conformation in cell-fate decisions. *Nature*. 2019;569:345–54.
53. Schoft VK, Chumak N, Mosiolek M, Slusarz L, Komnenovic V, Brownfield L, Twell D, Kakutani T, Tamaru H. Induction of RNA-directed DNA methylation upon decondensation of constitutive heterochromatin. *EMBO Rep*. 2009;10:1015–21.
54. Zheng Y, Zhang L, Jin L, Zhang P, Li F, Guo M, Gao Q, Zeng Y, Li M, Zeng W. Unraveling three-dimensional chromatin structural dynamics during spermatogonial differentiation. *J Biol Chem*. 2022;298: 101559.
55. Galbraith DW, Harkins KR, Maddox JM, Ayres NM, Sharma DP, Firoozabady E. Rapid Flow Cytometric Analysis of the Cell-Cycle in Intact Plant-Tissues. *Science*. 1983;220:1049–51.
56. Cyprys P, Lindemeier M, Sprunck S. Gamete fusion is facilitated by two sperm cell-expressed DUF679 membrane proteins. *Nat Plants*. 2019;5:253–7.
57. Chumak N, Mosiolek M, Schoft VK. Sample Preparation and Fractionation of *Arabidopsis thaliana* Sperm and Vegetative Cell Nuclei by FACS. *Bio Protoc*. 2015;5: e1664.
58. Lando D, Stevens TJ, Basu S, Laue ED. Calculation of 3D genome structures for comparison of chromosome conformation capture experiments with microscopy: An evaluation of single-cell Hi-C protocols. *Nucleus*. 2018;9:190–201.
59. Du Z, Zheng H, Huang B, Ma R, Wu J, Zhang X, He J, Xiang Y, Wang Q, Li Y, et al. Allelic reprogramming of 3D chromatin architecture during early mammalian development. *Nature*. 2017;547:232–5.

60. Zhang C, Xu Z, Yang S, Sun G, Jia L, Zheng Z, Gu Q, Tao W, Cheng T, Li C, Cheng H. tagHi-C Reveals 3D Chromatin Architecture Dynamics during Mouse Hematopoiesis. *Cell Rep.* 2020;32: 108206.
61. Zhou J, Ma J, Chen Y, Cheng C, Bao B, Peng J, Sejnowski TJ, Dixon JR, Ecker JR. Robust single-cell Hi-C clustering by convolution- and random-walk-based imputation. *Proc Natl Acad Sci U S A.* 2019;116:14011–8.
62. Hao Y, Hao S, Andersen-Nissen E, Mauck WM 3rd, Zheng S, Butler A, Lee MJ, Wilk AJ, Darby C, Zager M, et al. Integrated analysis of multimodal single-cell data. *Cell.* 2021;184:3573–87.
63. Chen S, Zhou Y, Chen Y, Gu J. fastp: an ultra-fast all-in-one FASTQ preprocessor. *Bioinformatics.* 2018;34:884–90.
64. Servant N, Varoquaux N, Lajoie BR, Viara E, Chen CJ, Vert JP, Heard E, Dekker J, Barillot E. HiC-Pro: an optimized and flexible pipeline for Hi-C data processing. *Genome Biol.* 2015;16:259.
65. Durand NC, Robinson JT, Shamim MS, Machol I, Mesirov JP, Lander ES, Aiden EL. Juicebox Provides a Visualization System for Hi-C Contact Maps with Unlimited Zoom. *Cell Syst.* 2016;3:99–101.
66. Naish M, Alonge M, Wlodzimierz P, Tock AJ, Abramson BW, Schmücker A, Mandáková T, Jamge B, Lambing C, Kuo P, et al. The genetic and epigenetic landscape of the Arabidopsis centromeres. *Science.* 2021;374:eabi7489.
67. Ramirez F, Bhardwaj V, Arrigoni L, Lam KC, Gruning BA, Villaveces J, Habermann B, Akhtar A, Manke T. High-resolution TADs reveal DNA sequences underlying genome organization in flies. *Nat Commun.* 2018;9:189.
68. Heinz S, Benner C, Spann N, Bertolino E, Lin YC, Laslo P, Cheng JX, Murre C, Singh H, Glass CK. Simple combinations of lineage-determining transcription factors prime cis-regulatory elements required for macrophage and B cell identities. *Mol Cell.* 2010;38:576–89.
69. Kruse K, Hug CB, Vaquerizas JM. FAN-C: a feature-rich framework for the analysis and visualisation of chromosome conformation capture data. *Genome Biol.* 2020;21:303.
70. Akdemir KC, Chin L. HiCPlotter integrates genomic data with interaction matrices. *Genome Biol.* 2015;16:198.
71. Khan A, Mathelier A. Intervene: a tool for intersection and visualization of multiple gene or genomic region sets. *BMC Bioinformatics.* 2017;18:287.
72. Stempor P, Ahringer J. SeqPlots - Interactive software for exploratory data analyses, pattern discovery and visualization in genomics. *Wellcome Open Res.* 2016;1:14.
73. Kim D, Paggi JM, Park C, Bennett C, Salzberg SL. Graph-based genome alignment and genotyping with HISAT2 and HISAT-genotype. *Nat Biotechnol.* 2019;37:907–15.
74. Danecek P, Bonfield JK, Liddle J, Marshall J, Ohan V, Pollard MO, Whitwham A, Keane T, McCarthy SA, Davies RM, Li H. Twelve years of SAMtools and BCFtools. *Gigasci.* 2021;10:gjab008.
75. Pertea M, Kim D, Pertea GM, Leek JT, Salzberg SL. Transcript-level expression analysis of RNA-seq experiments with HISAT, StringTie and Ballgown. *Nat Protoc.* 2016;11:1650–67.
76. Love MI, Huber W, Anders S. Moderated estimation of fold change and dispersion for RNA-seq data with DESeq2. *Genome Biol.* 2014;15:550.
77. Ramirez F, Ryan DP, Gruning B, Bhardwaj V, Kilpert F, Richter AS, Heyne S, Dundar F, Manke T. deepTools2: a next generation web server for deep-sequencing data analysis. *Nucleic Acids Res.* 2016;44:W160–5.
78. Langmead B, Salzberg SL. Fast gapped-read alignment with Bowtie 2. *Nat Methods.* 2012;9:357–9.
79. Neph S, Kuehn MS, Reynolds AP, Haugen E, Thurman RE, Johnson AK, Rynes E, Maurano MT, Vierstra J, Thomas S, et al. BEDOPS: high-performance genomic feature operations. *Bioinformatics.* 2012;28:1919–20.
80. Song Z, Xia Q, Yang M, Yang T, Liu Y, Wang D, Shu J, Liu Z, Chi Y, Xu H, Xing D, Zhou Y. Dynamic changes in 3D chromatin structure during male gametogenesis in Arabidopsis thaliana. *PRJEB71351*. European Nucleotide Archive. <https://www.ebi.ac.uk/ena/browser/view/PRJEB71351> (2025).
81. Zhu D, Wen Y, Yao W, Zheng H, Zhou S, Zhang Q, Qu LJ, Chen X, Wu Z. Distinct chromatin signatures in the Arabidopsis male gametophyte. *PRJEB47676*. European Nucleotide Archive. <https://www.ebi.ac.uk/ena/browser/view/PRJEB47676> (2023).
82. Zhu D, Wen Y, Yao W, Zheng H, Zhou S, Zhang Q, Qu LJ, Chen X, Wu Z. Distinct chromatin signatures in the Arabidopsis male gametophyte. *PRJEB47677*. European Nucleotide Archive. <https://www.ebi.ac.uk/ena/browser/view/PRJEB47677> (2023).
83. Borg M, Papareddy RK, Dombey R, Axelsson E, Nodine MD, Twell D, Berger F. Epigenetic reprogramming rewires transcription during the alternation of generations in Arabidopsis. *PRJNA649438*. Sequence Read Archive. <https://www.ncbi.nlm.nih.gov/bioproject/PRJNA649438> (2021).
84. Yin X, Romero-Campero FJ, Yang M, Baile F, Cao Y, Shu J, Luo L, Wang D, Sun S, Yan P, Gong Z, Mo X, Qin G, Calonje M, Zhou Y. Binding by the Polycomb complex component BMI1 and H2A monoubiquitination shape local and long-range interactions in the Arabidopsis genome. *PRJEB52473*. European Nucleotide Archive. <https://www.ebi.ac.uk/ena/browser/view/PRJEB52473> (2023).
85. Buttress T, He S, Wang L, Zhou S, Saalbach G, Vickers M, Li G, Li P, Feng X. Histone H2B.8 compacts flowering plant sperm through chromatin phase separation. *PRJNA677963*. Sequence Read Archive. <https://www.ncbi.nlm.nih.gov/bioproject/PRJNA677963> (2022).

Publisher's Note

Springer Nature remains neutral with regard to jurisdictional claims in published maps and institutional affiliations.